



**Numerical Simulation of Target
Microexplosion Dynamics for the LIBRA-SP
Inertial Confinement Fusion Reactor**

**J.J. MacFarlane, G.A. Moses, P. Wang,
M.E. Sawan, R.R. Peterson**

December 1994

UWFDM-973

***FUSION TECHNOLOGY INSTITUTE
UNIVERSITY OF WISCONSIN
MADISON WISCONSIN***

DISCLAIMER

This report was prepared as an account of work sponsored by an agency of the United States Government. Neither the United States Government, nor any agency thereof, nor any of their employees, makes any warranty, express or implied, or assumes any legal liability or responsibility for the accuracy, completeness, or usefulness of any information, apparatus, product, or process disclosed, or represents that its use would not infringe privately owned rights. Reference herein to any specific commercial product, process, or service by trade name, trademark, manufacturer, or otherwise, does not necessarily constitute or imply its endorsement, recommendation, or favoring by the United States Government or any agency thereof. The views and opinions of authors expressed herein do not necessarily state or reflect those of the United States Government or any agency thereof.

**Numerical Simulation of Target Microexplosion Dynamics
for the LIBRA-SP Inertial Confinement Fusion Reactor**

J. J. MacFarlane, G. A. Moses, P. Wang, M. E. Sawan, and R. R. Peterson

Fusion Technology Institute
1500 Johnson Drive
University of Wisconsin
Madison, WI 53706

December 1994

UWFDM-973

1. Introduction

High-gain targets to be used in inertial confinement fusion (ICF) power reactors are expected to release $\sim 10^2 - 10^3$ MJ of energy in the form of x-rays, energetic ions, and neutrons [1-3]. This energy originates in the central, highly compressed core of an ICF target due to fusion of deuterium (D) and tritium (T). The primary fusion products of D-T reactions are α -particles (^4He) and 14 MeV neutrons, while secondary products from D-D and D- ^3He reactions include lower energy neutrons, gamma photons, and charged particles (^3He , T, and protons). Because charged particles have relatively short mean free paths, the bulk of this energy is deposited within the target. Energy is transferred from the hot central fuel region to the outer layers of the target by radiation, conduction, and mass motion (kinetic energy) leading to release of x-rays and ion debris. On the other hand, a significant fraction of the neutrons escape the target. It is important to understand the partitioning of energy during the target explosion phase because it provides information critical to the design of ICF target chambers.

Below, we describe calculations of the fusion burn and explosion energetics of the ICF target for the LIBRA-SP light ion fusion reactor design [4]. In this design, the spherical target is irradiated with 24 Li ion beams (12 prepulse and 12 full power) containing a total energy of 7.2 MJ. The peak beam power on target is 330 TW and the pulse width of the full power beams is 20 ns. Internal pulse shaping of the x-ray flux onto the capsule [5] is expected to lead to a gain of about 80, thus producing a total target yield of approximately 550-600 MJ.

The purpose of this investigation is to begin to address quantitatively the *explosion* dynamics of the LIBRA target. It is anticipated that the physics of the *implosion* phase will be addressed in a future study. To study the explosion dynamics, we start with an already-imploded configuration which represents a reasonable representation of the target plasma conditions at the instant of ignition. The evolution of the target breakup is then simulated using the PHD-IV radiation-hydrodynamics code [6]. This code computes the

Table 1. LIBRA-SP Target and Ion Beam Parameters

	LIBRA-SP
Total absorbed beam energy	7.2 MJ
Peak beam power (main + prepulse)	330 TW
Hohlraum radius	0.7 cm
Yield	589 MJ
Peak beam intensity	54 TW/cm ²
Target gain	82

time-dependent fusion burn and energy transport within the target. The calculations also utilize new equation of state (EOS) and opacity models developed at Wisconsin [7]. The primary goal of the calculations is to make quantitative predictions for the time-dependent target x-ray flux and ion debris energy. These quantities can then be used to determine the response of the target chamber first wall to the target microexplosion.

The original LIBRA [1] and LIBRA-LiTE [8] designs utilized scaled versions of targets originally designed for heavy ion beam reactors [2] because of classification issues in the U.S. However, recent declassification of light ion targets now allows the use of more realistic target configurations. The LIBRA-SP target design, shown in Fig. 1, is based on the target design for the Laboratory Microfusion Facility (LMF) [9]. Several of the LIBRA-SP target parameters are listed in Table 1. The two targets are designed with the same strategy. The beam ions penetrate the Hohlraum case and deposit in a low density carbon or plastic foam that is doped with high Z impurity to control the deposition profile. The foam heats to 200-300 eV, creating the drive radiation which is confined by the Hohlraum case. The radiation burns through the pulse-shaping layer around the capsule, shortening the pulse of radiation in the process. The capsule is then driven to implosion by the reshaped radiation pulse. This design has been studied in detail for the LMF target [9]. The predicted gain for the LIBRA-SP design is compared with that of other ICF reactor conceptual design studies in Fig. 2.

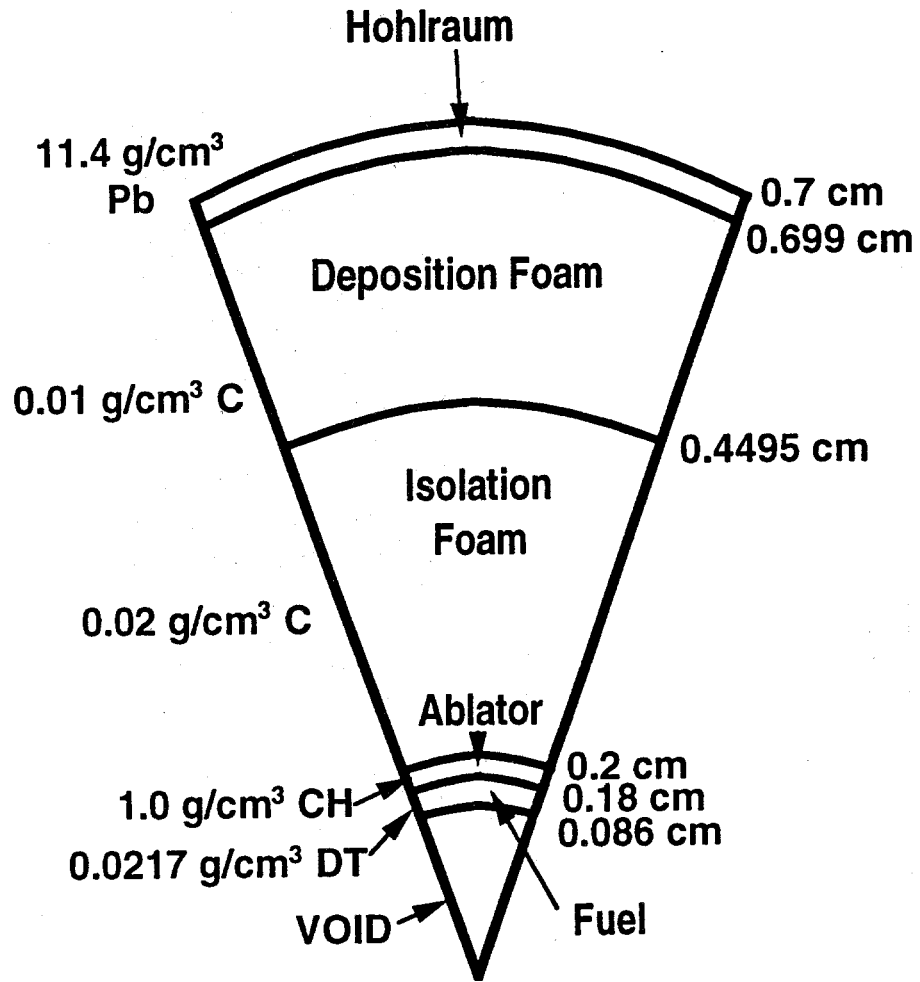


Figure 1. Schematic of initial target configuration for LIBRA-SP.

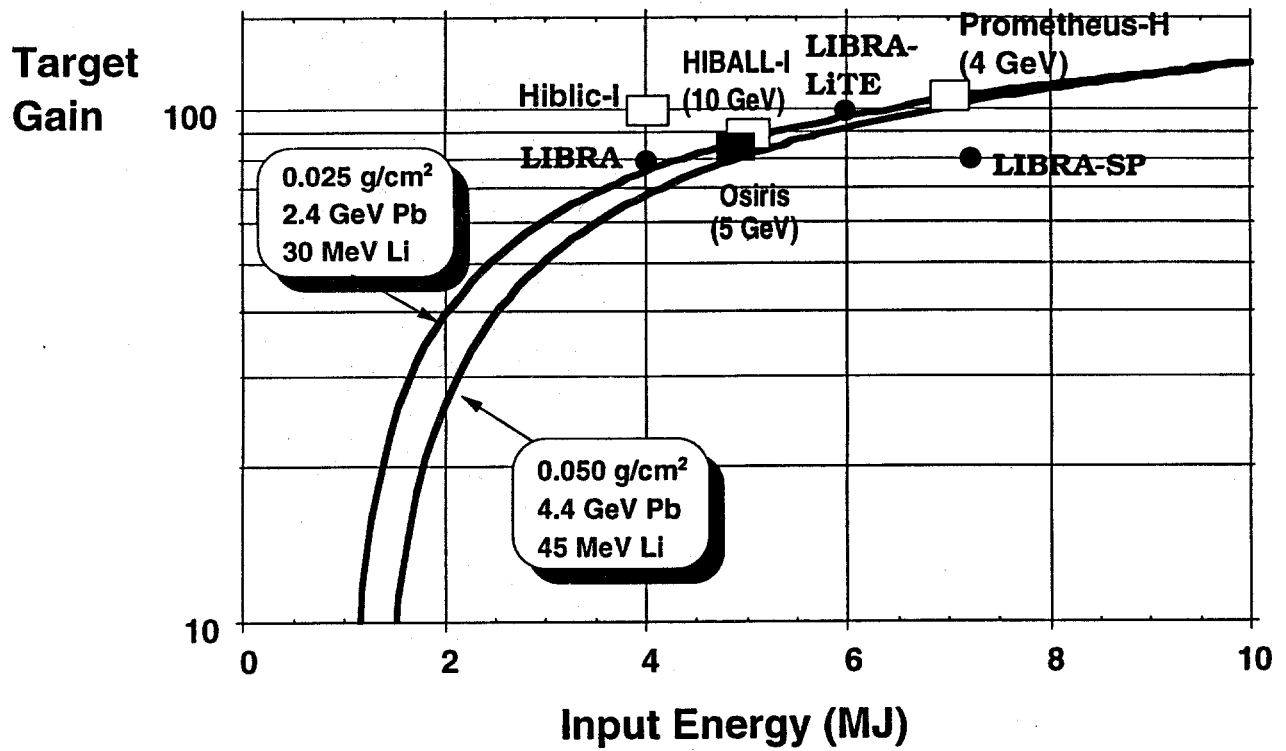


Figure 2. Comparison of target gains from several ICF reactor conceptual design studies. The performance of targets that rely on internal pulse shaping is slightly degraded from other ICF target designs.

2. Physics Models

2.1. PHD-IV Target Simulation Code

PHD-IV [6] is a plasma radiation-hydrodynamics code with models for ion beam energy deposition and fusion burn designed to model ICF target physics processes. It is a 1-D Lagrangian code which solves the single-fluid equation of motion with pressure contributions from electrons, ions, radiation, and fast charged particle reaction products. Energy transfer in the plasma is treated with a 2-temperature model — i.e., separate ion and electron temperatures. Thermal conduction through each species is treated using Spitzer’s form of the thermal conductivity. The electron conductivity is flux-limited. Radiation emission and absorption terms couple the electron temperature equation to the radiation transport equations. In addition, the electron and ion temperature equations contain source terms that couple them to the ion beam energy deposition calculation and the energy deposited from the fusion reactions.

The simulations for the LIBRA-SP target utilize a hybrid equation of state model which couples high-density thermodynamic properties calculated using a muffin-tin model to lower density properties which are computed using a detailed configuration accounting model. Multigroup opacities are computed using the EOSOPA code (see below). Radiation is transported using a multigroup flux-limited diffusion model [10]. A total of 200 frequency groups was used in the simulation described below. The time-dependent radiation energy density equations are solved using implicit finite difference techniques.

Fusion reaction equations for DT, DD, and D-³He are solved and the reaction products are transported and slowed using a time-dependent particle tracking algorithm. In addition, PHD-IV includes an ion beam energy deposition package to model the time which includes contributions to the stopping power from both bound and free electrons. However, this latter package was not required for the microexplosion simulation described below.

2.2. EOS and Opacity Models

The equation of state covers a wide domain of densities and temperatures. It consists primarily of three contributions: (1) the zero-temperature isotherm, (2) a thermal electronic component, and (3) a thermal ionic part. We have used a hybrid model in the equation of state calculations: a detailed configuration accounting (DCA) model is used for the low-density, high-temperature regime, while a “muffin-tin” model [11] is used for the high-density regime.

In the detailed configuration accounting model, each isolated ion in the plasma is in equilibrium with free electrons. Plasma effects on each atomic system are considered as perturbations. Ion abundances and level occupation numbers are obtained from detailed ionization balance calculations. In our LIBRA-SP calculations, the EOS’s are obtained for plasmas with local thermodynamic equilibrium (LTE) populations. Continuum lowering effects are accounted for in the opacity calculations using an occupation probability formalism [12]. The following contributions are included in the equations of state: (1) the translational energy of ions and atoms, (2) the energy of partially degenerate electrons, (3) configuration effects from Coulomb interactions (Debye-Hückel corrections), and (4) atomic internal contributions (excitations and ionizations).

The muffin-tin model is used to accurately compute the equation of state for high-density plasmas. It is applicable to electrons on the zero-temperature isotherm as well as for any finite temperature. It has much of the simplicity of an isolated atom model but captures much of the physics of the band-structure model. In particular, it provides an accurate description of cohesion and the behavior of solids under compression. This model also describes an isolated atom or an ion in equilibrium with an electron gas in low density cases. Hence the muffin-tin model smoothly connects high-density electron degenerate regime and low-density plasma regime. This smooth connection provides thermodynamic consistency of calculated equations of state over a wide domain of temperatures and densities.

Our hybrid model is designed to provide reliable equations of state over a wide range of temperatures and densities. Figure 3 shows our results for energy and pressure isotherms of aluminum. In the low-density regime, the nonlinear behavior due to ionization/excitation is clearly seen. The cohesive, degenerate, and pressure ionization effects are observed for the high-density regime. Figure 4 shows a comparison of calculated shock Hugoniot with experimental data for Al and Au. It can be seen that the agreement is good.

In order to be able to treat properly the transfer of radiation in LIBRA targets, it is necessary to have values of the opacity for both low-Z and high-Z elements in a wide range of conditions. Radiation is absorbed by atoms and ions via the following types of processes: (1) bound-bound transitions (line absorption); (2) bound-free transitions (photoionization); (3) free-free transitions (Bremsstrahlung); (4) scattering of photons by electrons. In principle, the calculations of opacity for low-Z and high-Z systems are the same. In practice, however, they must be treated differently. We use a detailed term accounting (DTA) method for low-Z systems, and use an unresolved transition array (UTA) model for high-Z systems.

For high-Z atomic systems, especially for the ions in electronic configurations with open d or f shells, each configuration contains a very large number of levels. As a consequence, the number of lines corresponding to the bound-bound transitions between these levels are so numerous that it is impractical to do detailed line accounting calculations. On the other hand, these lines are so closely packed that intrinsic broadening effects suffice to merge them together. Because of this characteristic of high-Z line spectra, an unresolved transition array (UTA) model [13] can be used to compute high-Z opacities. The UTA model uses an average transition between configuration-averaged atomic levels to represent the numerous possible transitions (the transition array) between configurations. The splitting effect of these lines is accounted for by using a line shape for each transition array which is determined from Slater integrals. It is very important to include line broadening due to this UTA effect. Figure 5 shows a comparison of gold opacities calculated with and without this broadening effect. The curve on the left was calculated with normal line

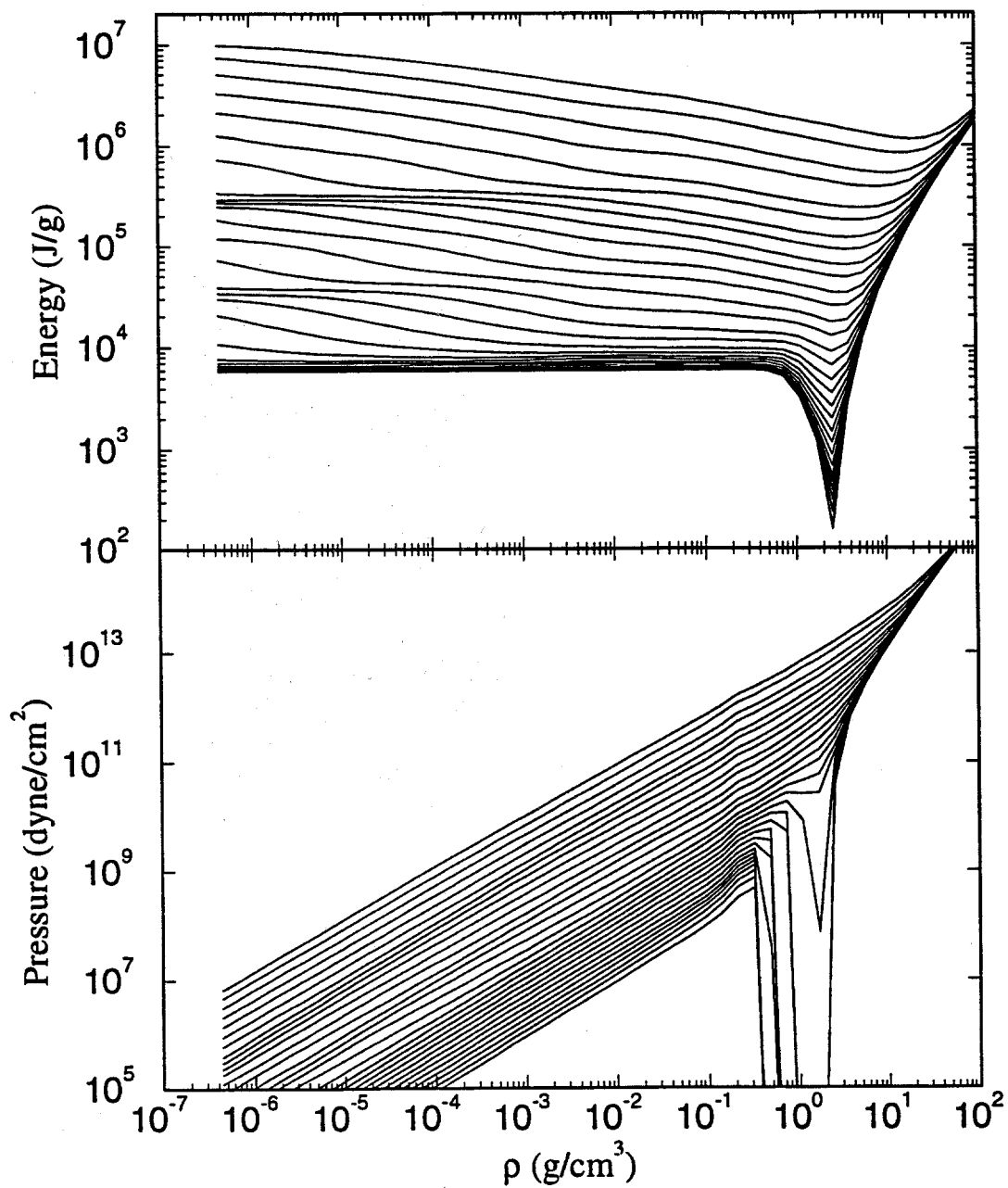


Figure 3. Energy and pressure isotherms calculated for Al using hybrid equation of state model.

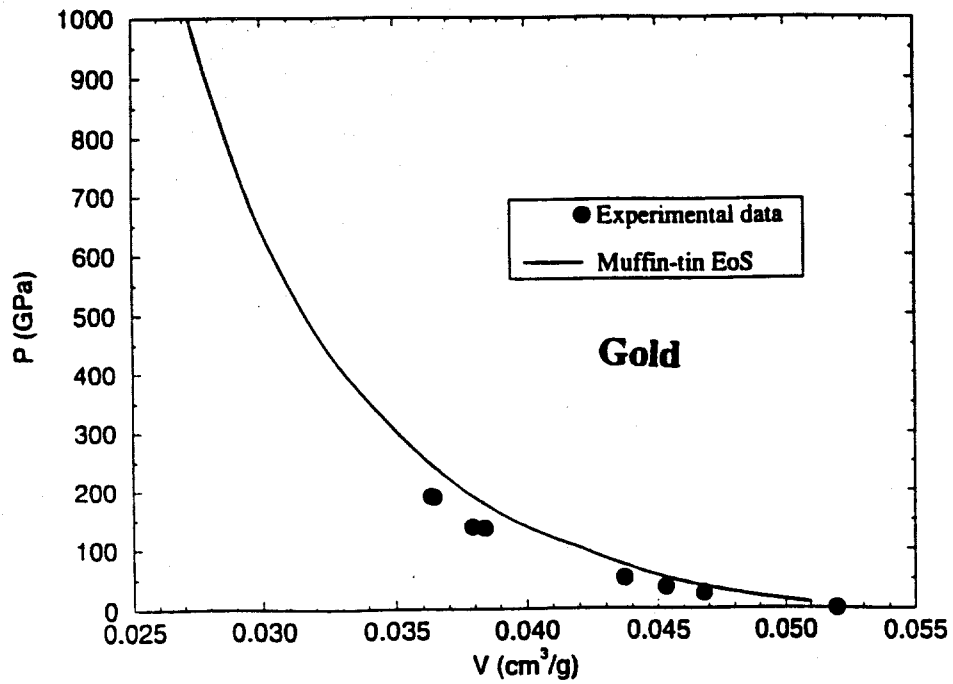
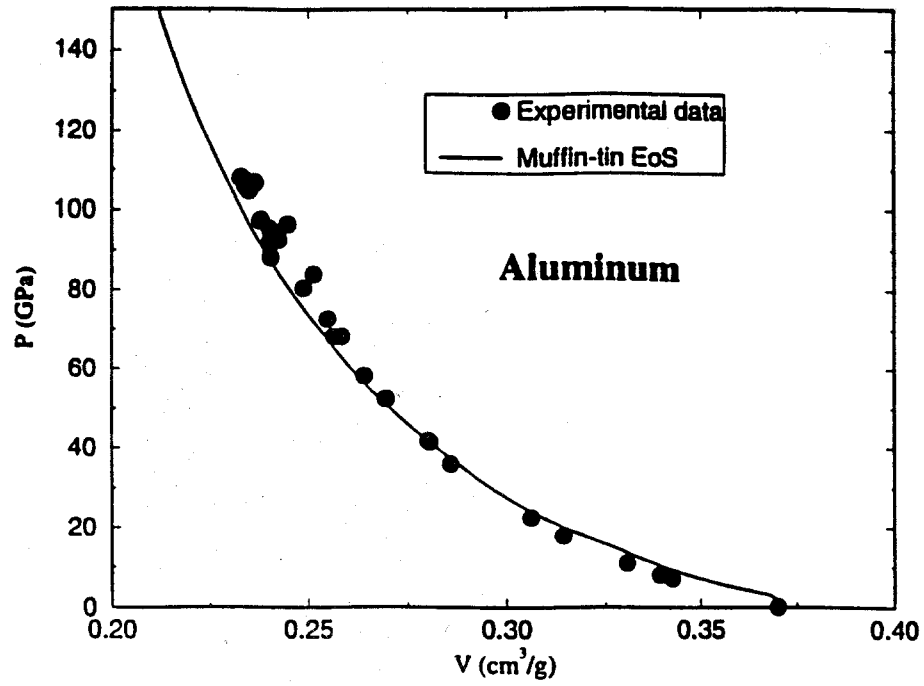


Figure 4. Comparison of calculated shock Hugoniot with experimental data for Al and Au.

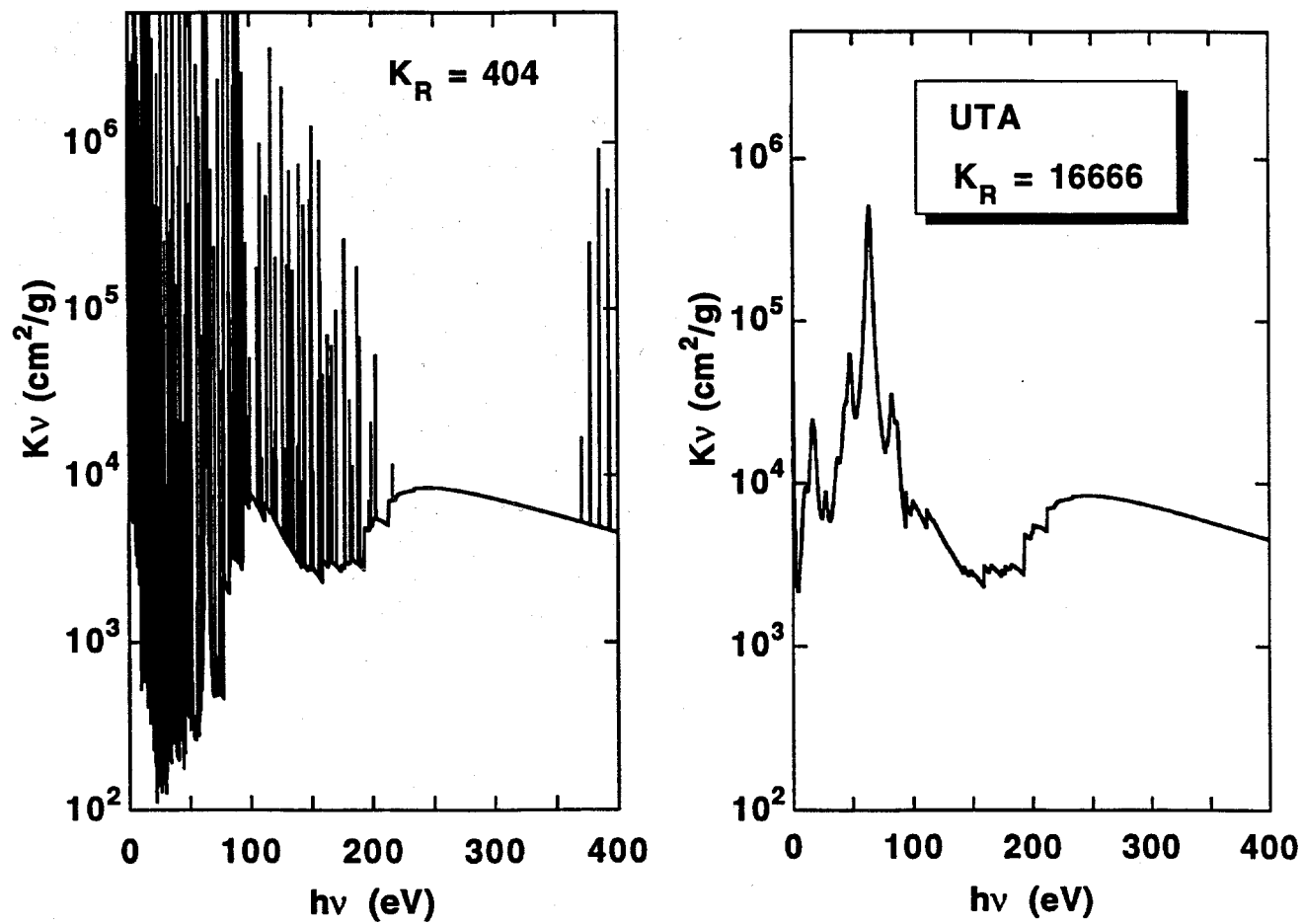


Figure 5. Frequency-dependence of Au opacity from calculations neglecting (left) and including (right) broadening due to UTA's.

shapes which include Doppler, natural, and electron impact broadening, while the curve on the right also includes UTA broadening. It is seen that the non-UTA result leads to a mean Rosseland opacity that is a factor of 40 lower than the UTA result. The UTA model is more accurate and is used in our Pb opacity calculations for the LIBRA target.

To assess the reliability of our opacity calculations, we have compared our results with other theoretical results [14]. In general, we find good agreement with some of the more reputable opacity codes (e.g., OPAL [15] and STA [16]).

3. Results

Conditions at the start of ignition assumed for the microexplosion simulation are shown in Fig. 6. At present, we simply assume these conditions can be roughly achieved using the beam parameters discussed above in conjunction with an x-ray internal pulse shaping scheme [9]. Clearly, however, a numerical simulation of the implosion is required to provide a more accurate target configuration at ignition.

The LIBRA-SP target is composed of 4 materials: the central DT fuel, a CH ablator, C deposition and isolation foams, and an outer Pb case (Hohlraum). At the start of the PHD-IV simulation, each of the material regions is assumed to have a uniform temperature and density, with the values indicated in Fig. 6. The exception to this is the DT fuel, which consists of a central hot spot surrounded by two other DT regions of successively higher density and lower temperature. The outer Pb region is assumed to have expanded by almost three orders of magnitude by the start of ignition. A total of 100 spatial zones was used in the simulation. At the start of the simulation, the areal density of the central hot spot is 0.3 g/cm^2 , while that of the entire DT fuel is 3.3 g/cm^2 . The fusion burn begins in the hot DT core which is initially at 8 keV. The burn region then propagates outward engulfing the entire DT region. By the end of the simulation a burn fraction of approximately 35% is achieved.

Results from the simulation are shown in Figs. 7 through 11. Figure 7 shows the time-dependent position of the Lagrangian zones, which indicate the material motion in

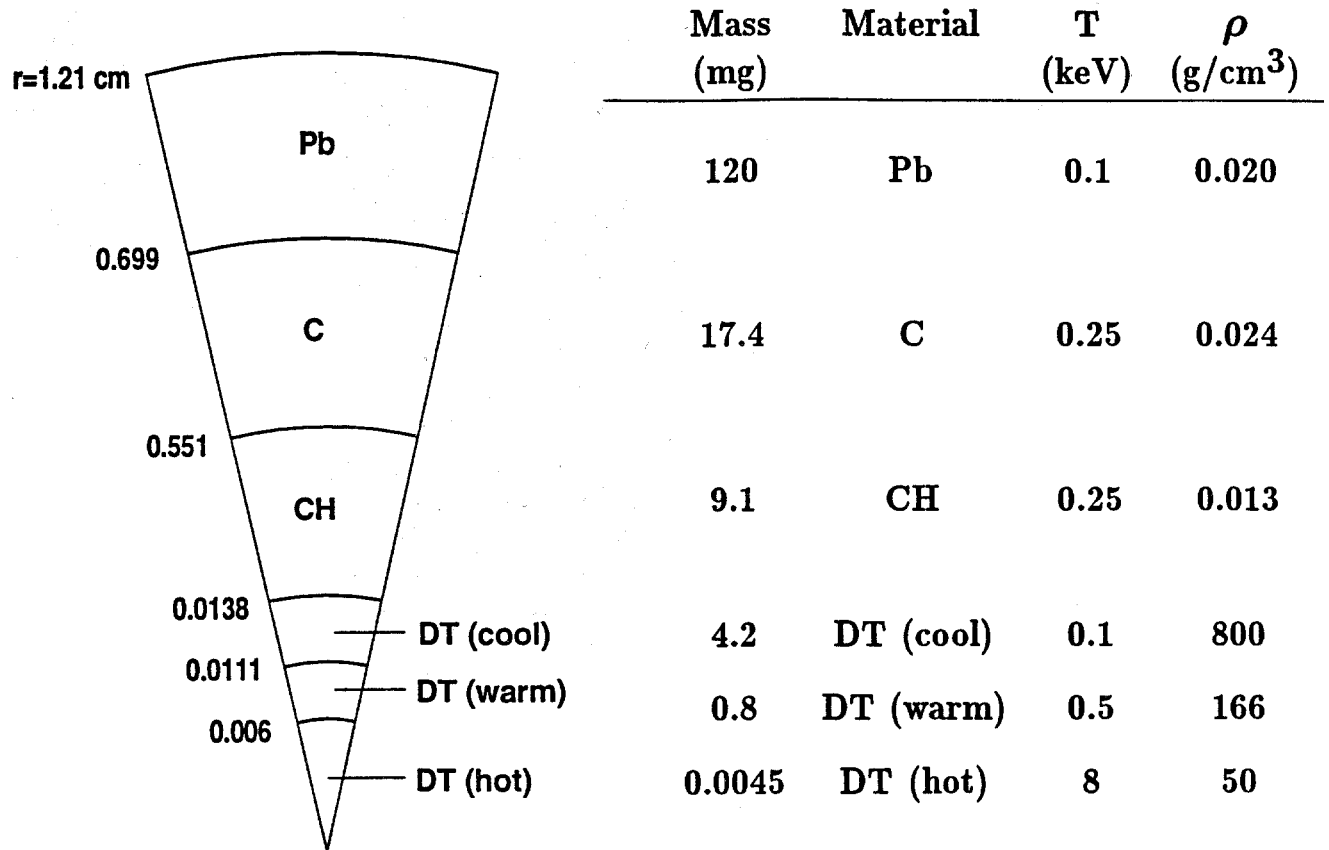


Figure 6. Conditions at the start of ignition assumed for the PHD-IV LIBRA-SP simulation.

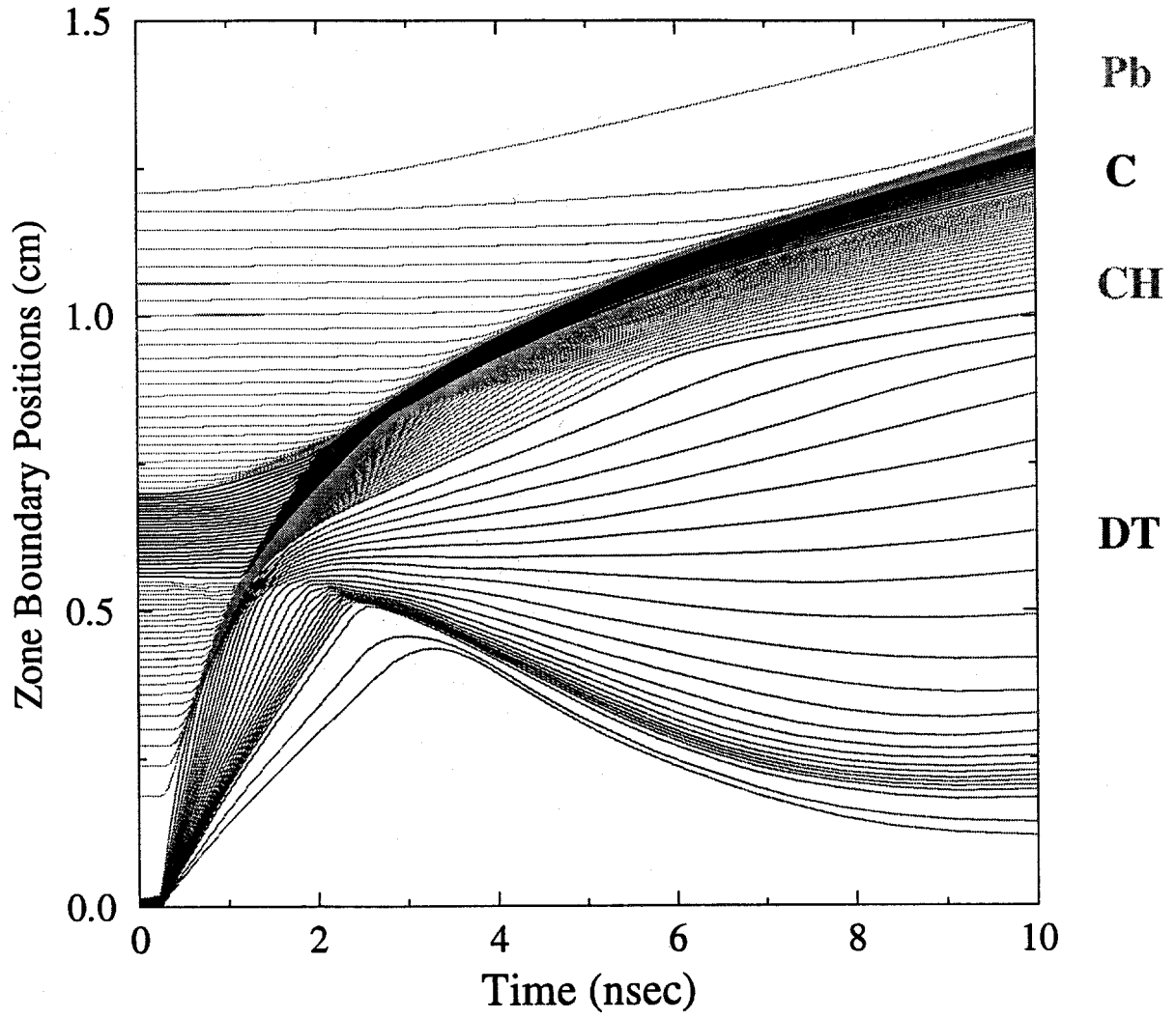


Figure 7. Time-dependence of Lagrangian zone boundaries.

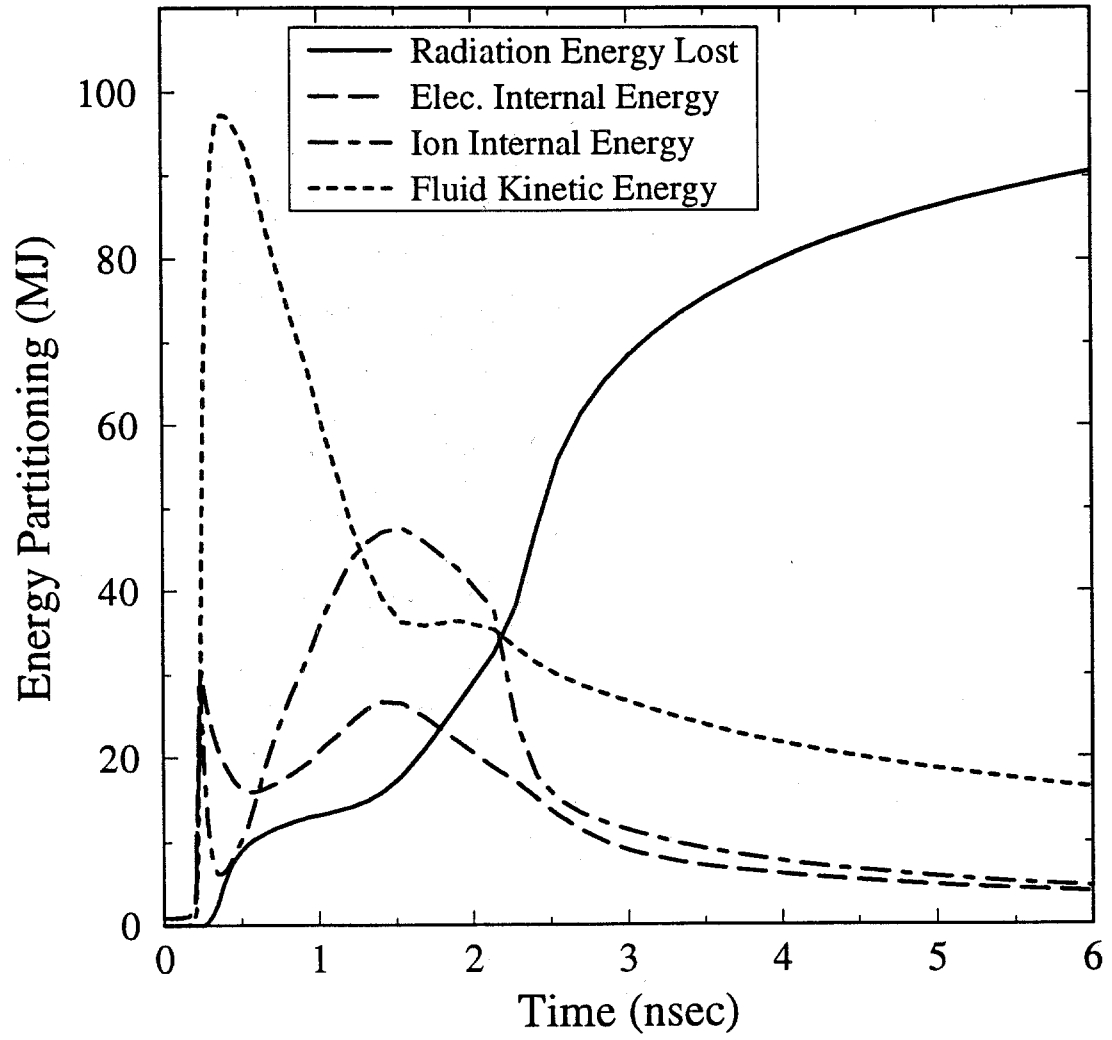


Figure 8. Time-dependence of energy partitioning in LIBRA-SP target.

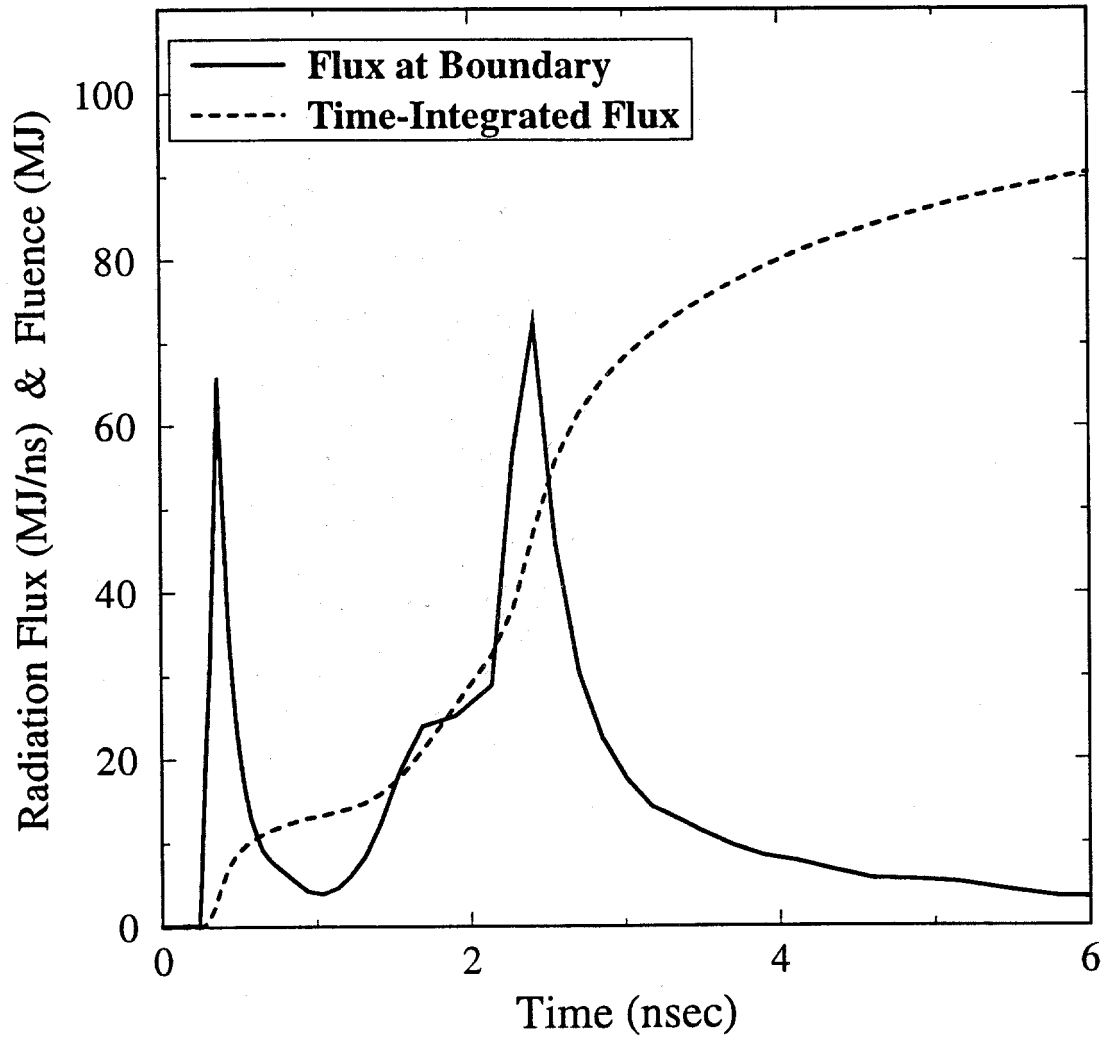


Figure 9. Time-dependent and time-integrated radiation power emitted from the boundary of the LIBRA-SP target.

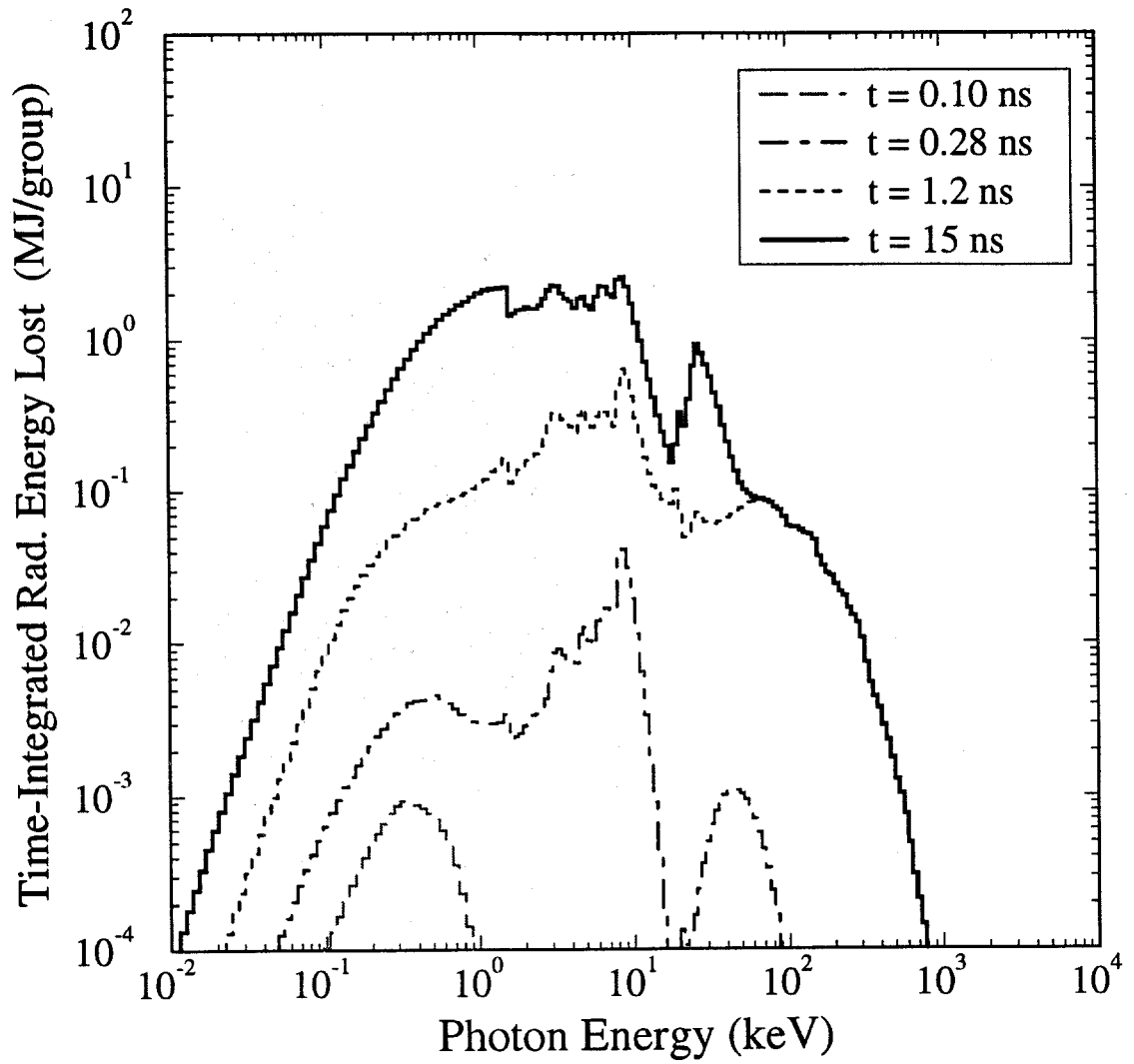


Figure 10. Time-integrated spectra of radiation emitted from the target boundary at several simulation times.

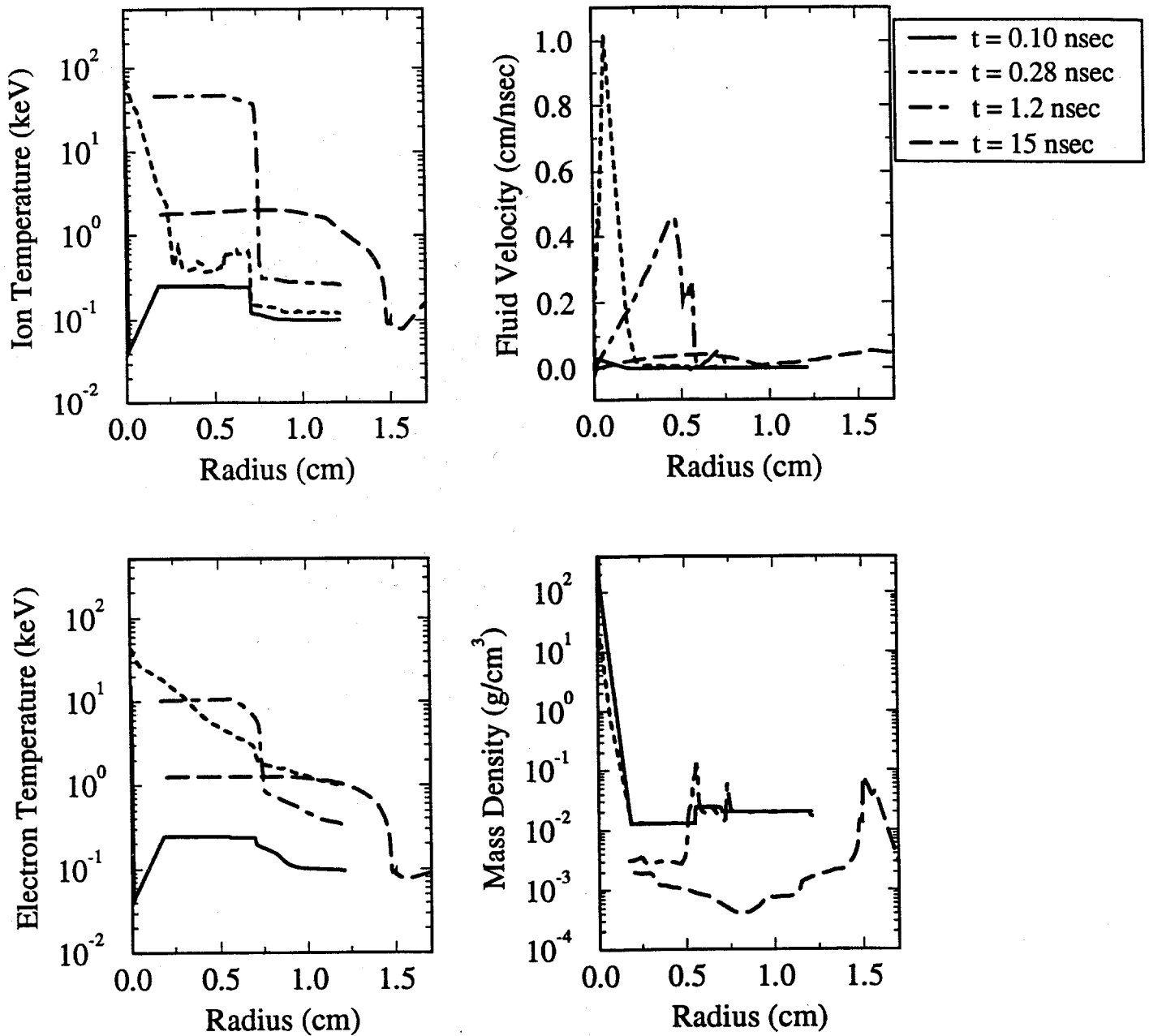


Figure 11. Radial profiles of ion temperature, electron temperature, fluid velocity, and mass density at several simulation times.

the target. Figures 8 and 9 describe the energy partitioning and radiation flux histories. Figure 10 shows time-integrated spectra for the radiation flux escaping the target at several simulation times. Figure 11 shows radial profiles for the ion and electron temperatures, fluid velocity, and mass density at several simulation times.

The fusion burn phase lasts approximately 200 ps and produces a peak ion temperature in the DT fuel of about 300 keV. The DT expands rapidly outward, converting its internal energy into kinetic energy. Note that at 0.4 ns, 98 MJ (or roughly 80% of the total α -particle energy released by the DT fuel) is in the form of kinetic energy (almost all of it in the DT). Figure 6 shows a strong shock propagating radially outward through the outer CH, C, and Pb regions. Shortly after the shock enters the Pb region, somewhat more than half of the DT kinetic energy has been converted back into internal energy throughout the target.

The radiation flux from the target is characterized by two main peaks (Fig. 8). The first occurs from about 0.2 to 0.5 ns, and is due to hard x-rays emitted directly from the high-temperature DT. By this time, the DT has a significantly larger radius than near the start of ignition, and therefore has a larger radiating surface area. By 1 ns, about 11% of the total α -particle energy generated during the burn phase (i.e., about 13 MJ) escapes the target in the form of hard x-rays. Figure 9 shows that virtually all hard x-rays with $h\nu \gtrsim 50$ keV are emitted by this time.

A burst of softer x-rays is emitted from the target from about 1.5 to 5 ns. These x-rays in large part originate in the Pb region, where electron temperatures reach as high as several keV during this time (see Fig. 10). By 5 ns, a total of 85 MJ has been radiated from the target, and by the end of the simulation ($t = 20$ ns) a total of 97 MJ of radiative energy has escaped the target. The frequency dependence of the escaping radiation (Fig. 9) shows the bulk of the radiation comes out between 10^{-1} and 10^2 keV, with the spectrum being clearly non-Planckian. The structure seen in the spectra is due to the fact that the temperature in the Pb region decreases as the radius increases. These features are thus

Table 2. Debris Ion Kinetic Energies

Species	Energy (MJ)	Energy per Ion (keV)
H	0.30	0.46
D	0.44	0.69
T	0.101	1.05
He ³	0.047	1.40
C	2.25	10.9
Pb	17.3	309

Table 3. Results for LIBRA-SP Target Burn Simulation

	PHD-IV Results	Corrected for Neutron Reabsorption
Total yield	589 MJ	589 MJ
Neutron yield	472 MJ	383 MJ
X-ray yield	97 MJ	167 MJ
Debris ion yield	20 MJ	35 MJ
Energy lost in endoergic reactions	–	4 MJ

due to absorption (as opposed to emission), which result from cooler regions absorbing radiation emitted from the higher temperature Pb at smaller radii. In particular, the Pb M-shell and L-shell photoabsorption edges can be seen near 1.6 and 10 keV, respectively.

By the end of the simulation a total of 20 MJ remains in the form of kinetic (debris ion) energy. The partitioning of the energy between the various target ion species in the PHD-IV simulation is shown in Table 2. The debris ion energy, along with the time- and frequency-dependent x-ray spectra, are then used in the LIBRA-SP target chamber simulations to determine the response of the PERIT units and LiPb liquid jet shield to the target explosion. Note that the results listed in Table 2 do not include the effects of neutron energy deposition within the target.

The overall partitioning of energy at the end of the PHD-IV simulation is shown in Table 3. Also shown in the right column are the values corrected for the redeposition of neutron energy within the target. Details of the neutron transport calculation are discussed

Table 4. Target Data at Ignition

Region	Material	Density (g/cm ³)	Radius Range (cm)
1	DT	230	0-0.0173
2	CH	0.013	0.0173-0.55
3	C	0.024	0.55-0.6983
4	Pb	11.4	0.6983-0.7

in the next section. Overall, approximately 65% of the total energy released by the high-gain target escapes the target in the form of neutrons, while the x-ray and debris ion energy account for 28% and 6% of the energy release, respectively.

3.1. Target Neutronics

The initial split of energy from a DT fusion reaction is one 14.1 MeV neutron and one 3.5 MeV alpha particle. In an inertial confinement fusion reactor, the DT fuel is heated and compressed to extremely high densities before it ignites. Therefore, neutron fuel interactions cannot be neglected. This results in significant softening of the neutron spectrum as a result of elastic and inelastic collisions with the target constituent materials. In addition, neutron multiplication occurs as a result of (n,2n) and (n,3n) reactions and gamma photons are produced. The energy deposited by the neutrons and gamma photons heats the target and ultimately takes the form of radiated x-rays from the hot plasma and expanding ionic debris.

Neutronics calculations have been performed for the LIBRA-SP target using the one-dimensional discrete ordinates code ONEDANT [17]. The LIBRA-SP target utilizes 5 mg of DT fuel. Although the DT fuel areal density (ρR) value changes during ignition, a value of 4 g/cm² is used in the target neutronics calculations. This is representative of the temporal average during ignition and burn. The target data at ignition used in the calculations are given in Table 4. The calculations were performed using spherical geometry and 30 neutron - 12 gamma group cross section data based on the ENDF/B-VI nuclear

Table 5. Nuclear Energy Deposition in Target

Region 1	2.53896 MeV/DT fusion
Region 2	0.00345 MeV/DT fusion
Region 3	0.00039 MeV/DT fusion
Region 4	0.00002 MeV/DT fusion
Total	2.54282 MeV/DT fusion

data evaluation [18]. A uniform 14.1 MeV neutron source was used in the compressed DT fuel zone.

Due to (n,2n) and (n,3n) reactions occurring in the target, 1.073 neutrons are emitted from the target for each DT fusion reaction. These neutrons carry an energy of 11.43 MeV implying that the average energy of neutrons emitted from the target is 10.65 MeV. It is interesting to note that only 61.2% of the neutrons emitted from the target are uncollided 14.1 MeV neutrons. For each DT fusion reaction, 0.0005 gamma photons are emitted from the target with an average energy of 2.4 MeV. The energy spectra of neutrons and gamma photons emitted from the LIBRA-SP target are shown in Figs. 12 and 13, respectively.

The total energy deposited by neutrons and gamma photons in the target was calculated to be 2.543 MeV per DT fusion. Almost all of the energy is deposited in the DT fuel zone as demonstrated by the results in Table 5. This is a direct result of the relatively large ρR value for the DT fuel region. When the 3.5 MeV energy carried by the alpha particle emerging from the fusion reaction is added, a total energy of 6.043 MeV per DT fusion is found to be carried by x-rays and target debris following the microexplosion. Performing an energy balance for the target indicates that 0.127 MeV of energy is lost in endoergic reactions per DT fusion. The detailed partitioning of the energy produced from the target is listed in Table 6. For the LIBRA-SP DT fuel yield of 589 MJ, the target yield is calculated to be 584.8 MJ. The neutron and gamma yields are 382.5 and 0.04 MJ, respectively, while the combined x-ray and debris yield is 202.3 MJ.

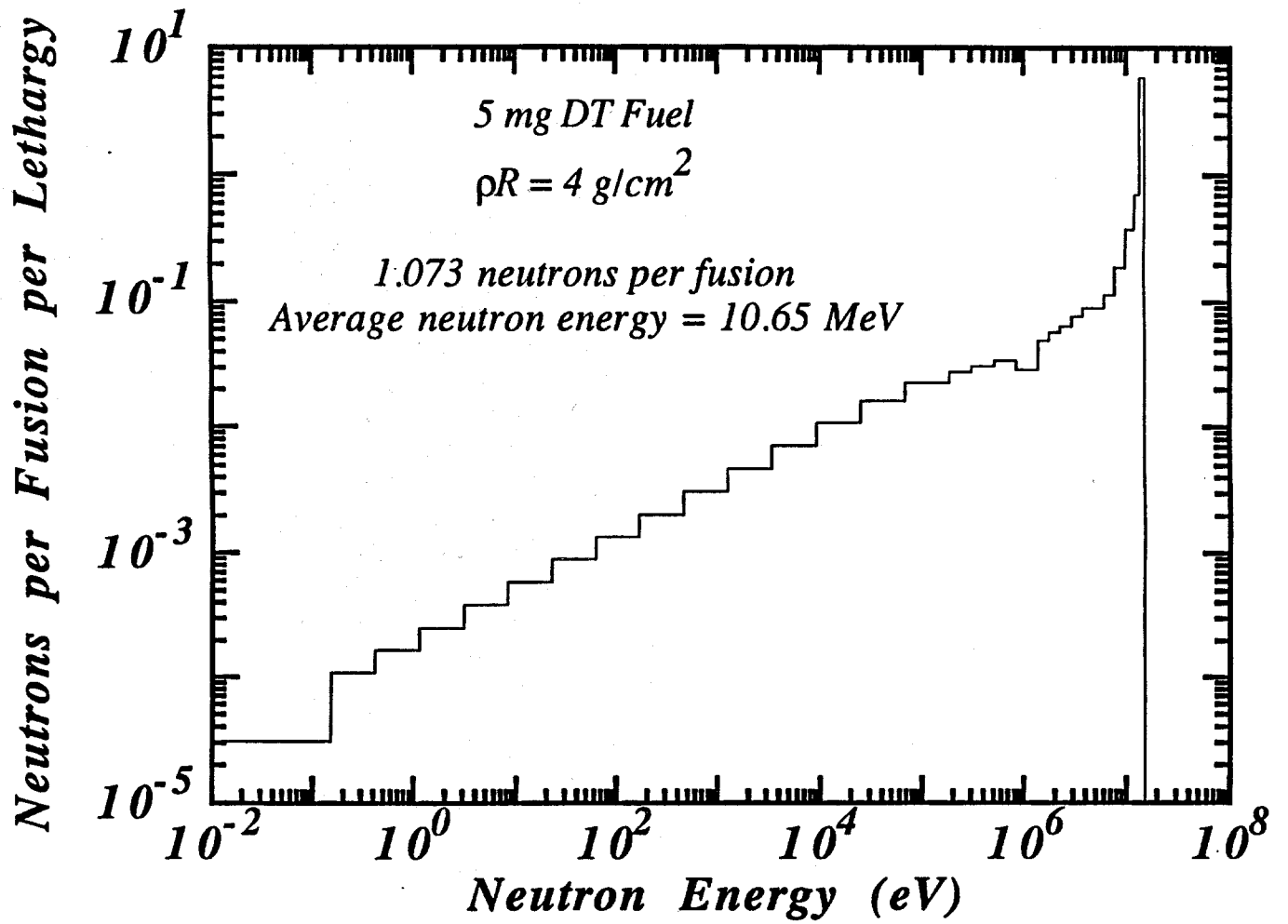


Figure 12. Energy spectrum of neutrons emitted from the LIBRA-SP target.

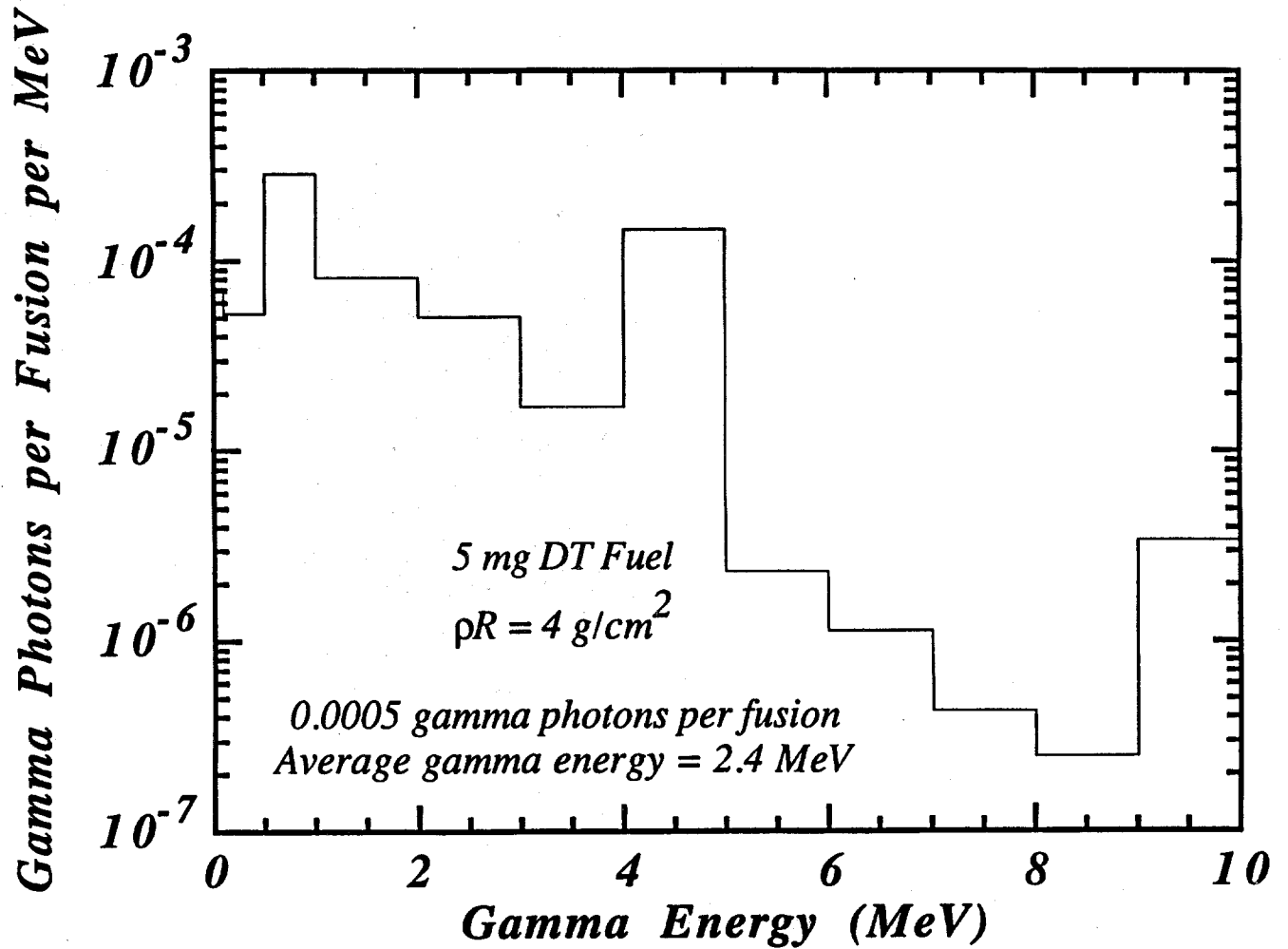


Figure 13. Energy spectrum of gamma photons emitted from LIBRA-SP target.

Table 6. Energy Partitioning from LIBRA-SP Target

Fusion energy	17.6 MeV/DT fusion
Energy carried by neutrons	11.429 MeV/DT fusion (64.94%)
Energy carried by gamma photons	0.001 MeV/DT fusion (0.006%)
Energy carried by x-rays and debris	6.043 MeV/DT fusion (34.34%)
Energy lost in endoergic reactions	0.127 MeV/DT fusion (0.72%)

4. Discussion and Future Work

We have performed preliminary calculations for the fusion burn and microexplosion of the LIBRA-SP target. Our results predict a total of 589 MJ of fusion energy is released, providing a gain of 82. The energy released in the form of neutrons is 383 MJ (65%). The bulk of this energy, because of the relatively long mean free paths of neutrons, is deposited in the LiPb blanket (PERIT units). Approximately 28% (167 MJ) of the target energy is emitted in the form of x-ray radiation, while 6% (35 MJ) is released in the form of debris ion kinetic energy. The x-ray and debris energy is stopped within the first few microns of the LiPb liquid jets located in front of the PERIT units. The response of the jets to the target x-ray and debris will be addressed elsewhere.

The purpose of these calculations has been to make quantitative predictions for the release of energy from high-gain ICF targets. However, much work remains to be done. Implosion calculations must be done to determine an accurate picture of the target conditions at the start of ignition. In addition, a more accurate, self-consistent simulation of the fusion target microexplosion requires the modeling of the reabsorption of neutron absorption within the target. It is anticipated that these items will be addressed in future work.

Acknowledgments

Funding for this work was provided by Sandia National Laboratory and Kernforschungszentrum Karlsruhe through Fusion Power Associates.

References

1. B. Badger et al., "LIBRA – A Light Ion Beam Fusion Conceptual Reactor Design," University of Wisconsin Fusion Technology Institute Report, UWFDM-800 (revised Feb. 1990).
2. B. Badger et al., "HIBALL – A Conceptual Heavy Ion Beam Driven Fusion Reactor Study, Preliminary Report," University of Wisconsin Fusion Technology Institute Report UWFDM-450 and KfK-3202.
3. I. N. Sviatoslavsky, et al., "A Near Symmetrically Illuminated Direct Drive Laser Fusion Power Reactor-SIRIUS-P," Eleventh Topical Meeting on the Technology of Fusion Energy, New Orleans, LA, June 1994.
4. G. L. Kulcinski, et al., "Evolution of Light Ion Driven Fusion Power Plants Leading to the LIBRA-SP Design," Eleventh Topical Meeting on the Technology of Fusion Energy, New Orleans, LA, June 1994.
5. R. Olson, private communication, 1994.
6. G. A. Moses, G. Magelssen, R. Israel, T. Spindler, and B. Goel, "PHD-IV – A Plasma Hydrodynamics, Thermonuclear Burn, Radiative Transfer Computer Code," University of Wisconsin Fusion Technology Institute Report UWFDM-194, Aug. 1985.
7. P. Wang, "EOSOPA – A Code for Computing the Equations of State and Opacities of High-Temperature Plasmas with Detailed Atomic Models," Fusion Power Associates Report FPA-93-8, Dec. 1993.

8. B. Badger et al., “LIBRA-LiTE – A Commercial Light Ion Fusion Power Plant,” FPA-91-4 and University of Wisconsin Fusion Technology Institute Report UWFDM-880, Dec. 1991.
9. R. Olson, private communication, 1994.
10. G. A. Moses, R. R. Peterson, and T. J. McCarville, “MF-FIRE – A Multifrequency Radiative Transfer Hydrodynamics Code,” *Comput. Phys. Commun.*, **36**, 249 (1985). R. R. Peterson, J. J. MacFarlane, and G. A. Moses, “CONRAD – A Combined Hydrodynamics-Condensation/Vaporization Computer Code,” University of Wisconsin Fusion Technology Institute Report UWFDM-670 (revised July 1988).
11. D. A. Liberman, *Phys. Rev.*, **B20**, 4981 (1979).
12. D. G. Hummer and D. Mihalas, *Ap. J.*, **331**, 794 (1988).
13. C. Bauche-Arnoulet, J. Bauche, and M. Klapisch, *Adv. At. Mol. Phys.*, **23**, 131 (1988).
14. P. Wang and J. J. MacFarlane, Third International Opacity Workshop and Code Comparison Study, MPI Quantenoptik, Garching, March 7-11, 1994.
15. C. A. Iglesias, F. J. Rogers, and B. G. Wilson, *Ap. J. Lett.*, **322**, L45 (1987).
16. A. Bar-Shalom, J. Oreg, W. H. Goldstein, D. Sharis, and A. Zigler, *Phys. Rev.*, **A40**, 3183 (1989).
17. R. O’Dell et al., “User’s Manual for ONEDANT: A Code Package for One-Dimensional, Diffusion-Accelerated, Neutral Particle Transport,” Los Alamos National Laboratory, LA-9184-M, 1989.
18. P. F. Rose, “ENDF/B-VI, The U.S. Evaluated Nuclear Data Library for Neutron Reaction Data,” Summary Documentation Report ENDF 201, U.S. National Nuclear Data Center, 1992.